

Spatial Preprocessing for Endmember Extraction

Maciel Zortea and Antonio Plaza, *Senior Member, IEEE*

Abstract—Endmember extraction is the process of selecting a collection of pure signature spectra of the materials present in a remotely sensed hyperspectral scene. These pure signatures are then used to decompose the scene into abundance fractions by means of a spectral unmixing algorithm. Most techniques available in the endmember extraction literature rely on exploiting the spectral properties of the data alone. As a result, the search for endmembers in a scene is conducted by treating the data as a collection of spectral measurements with no spatial arrangement. In this paper, we propose a novel strategy to incorporate spatial information into the traditional spectral-based endmember search process. Specifically, we propose to estimate, for each pixel vector, a scalar spatially derived factor that relates to the spectral similarity of pixels lying within a certain spatial neighborhood. This scalar value is then used to weigh the importance of the spectral information associated to each pixel in terms of its spatial context. Two key aspects of the proposed methodology are given as follows: 1) No modification of existing image spectral-based endmember extraction methods is necessary in order to apply the proposed approach. 2) The proposed preprocessing method enhances the search for image spectral endmembers in spatially homogeneous areas. Our experimental results, which were obtained using both synthetic and real hyperspectral data sets, indicate that the spectral endmembers obtained after spatial preprocessing can be used to accurately model the original hyperspectral scene using a linear mixture model. The proposed approach is suitable for jointly combining spectral and spatial information when searching for image-derived endmembers in highly representative hyperspectral image data sets.

Index Terms—Endmember extraction, hyperspectral data processing, spatial-spectral analysis, spectral mixture analysis.

I. INTRODUCTION

HYPERSPECTRAL imaging has been transformed from being a sparse research tool into a commodity product that is available to a broad user community [1]. The wealth of spectral information available from hyperspectral imaging instruments has opened new perspectives in many application domains, such as monitoring of environmental and urban processes or risk prevention and response, including—among others—tracking wildfires, detecting biological threats, and monitoring oil spills and other types of chemical contamination. Advanced hyperspectral instruments such as the National Aeronautics and Space Administration's Airborne Visible/Infrared Imaging Spectrometer (AVIRIS) [2] are now able to cover the wavelength region from 0.4 to 2.5 μm using more than 200

Manuscript received November 3, 2008; revised January 28, 2009. First published April 3, 2009; current version published July 23, 2009. This work was supported by the European Community's Marie Curie Research Training Networks Program under Contract MRTN-CT-2006-035927 [Hyperspectral Imaging Network (HYPER-I-NET)].

The authors are with the Department of Technology of Computers and Communications, University of Extremadura, 10071 Cáceres, Spain.

Color versions of one or more of the figures in this paper are available online at <http://ieeexplore.ieee.org>.

Digital Object Identifier 10.1109/TGRS.2009.2014945

contiguous spectral channels, each with a full-width at half-maximum of about 10 nm.

Several analytical tools have been developed for hyperspectral data processing in recent years, covering topics such as dimensionality reduction, classification, data compression, or spectral mixture analysis [3]–[5]. The underlying assumption governing clustering and classification techniques is that each pixel vector comprises the response of a single underlying material. However, if the spatial resolution of the sensor is not high enough to separate different materials, these can jointly occupy a single pixel, and the resulting spectral measurement will be a *mixed* pixel, i.e., a composite of the individual pure spectra [6]. To deal with this problem, linear spectral mixture analysis techniques first identify a collection of spectrally pure constituent spectra, which are often called *endmembers* in the literature, and then express the measured spectrum of each mixed pixel as a linear combination of endmembers weighed by fractions or abundances that indicate the proportion of each endmember present in the pixel [7].

Over the last decade, several algorithms have been developed for automatic or semiautomatic extraction of spectral endmembers [8]. Classic techniques include the pixel purity index [9], N-FINDR [10], iterative error analysis (IEA) [11], Optical Real-time Adaptive Spectral Identification System (ORASIS) [12], convex cone analysis [13], and an orthogonal subspace projection (OSP) technique in [14]. Other advanced techniques for endmember extraction have recently been proposed [15]–[21], but none of them considers spatial adjacency. However, one of the distinguishing properties of hyperspectral data is the multivariate information coupled with a 2-D (pictorial) representation amenable to image interpretation. Subsequently, most of the endmember extraction algorithms previously mentioned could benefit from an integrated framework in which both the spectral information and the spatial arrangement of pixel vectors are taken into account. To the best of our knowledge, only a few attempts existing in the literature aimed at including spatial information in the process of extracting spectral endmembers. Two of the most representative efforts in this direction are described here.

- 1) The automatic morphological endmember extraction [22] algorithm runs on a full data cube with no dimensional reduction and begins by searching the spatial neighborhoods around each pixel in the image for the most spectrally pure and mostly highly mixed pixel. This task is performed by using extended mathematical morphology operators [23] of dilation and erosion, respectively. Each spectrally pure pixel is assigned an “eccentricity” value, which is calculated as the spectral angle distance (SAD) between the most spectrally pure and the mostly highly mixed pixel for the given spatial neighborhood. This

process is iteratively repeated for larger spatial neighborhoods of up to a predetermined maximum size. At each iteration, the “eccentricity” values of the selected pixels are updated. The final endmember set is obtained by applying a threshold to the resulting grayscale “eccentricity” image. The final endmembers are extracted after a region growing process.

- 2) The spatial spectral endmember extraction (SSEE) [24] algorithm comprises four steps.
 - 1) It applies singular value decomposition to determine a set of eigenvectors that describe most of the spectral variance of image subsets.
 - 2) It projects the entire image data onto the compiled eigenvector set to determine a set of candidate endmember pixels.
 - 3) The algorithm analyzes the spatial and spectral characteristics of the candidate endmember set to average spectrally similar endmember candidates that are spatially related.
 - 4) Finally, the endmember set derived in the previous step is reordered based on the spectral angle, thus listing endmember candidates in order of spectral similarity (from highest to lowest similarity).

It is important to briefly discuss the use of spectral averaging in order to produce the final endmembers. It should be noted that averaging candidate pixels is a common practice in several endmember extraction methods, such as the IEA and SSEE, in which candidate endmember pixels that are spectrally similar are averaged to reduce the effects of noise and to average out the subtle spectral variability of a given class (thus generating a more representative endmember for the class as a whole). In this case, although the averaging process will likely change the original spectral signature of the endmember spectra, the averaging itself can be advantageous. However, another alternative that is pursued in this paper is to model the within-class spectral variability by directing the search for spectral endmembers to spatially homogeneous regions, in the hope of addressing three desirable features for an endmember extraction algorithm.

- 1) Spatial information may be used as a *guide* to effectively exploit spectral information.
- 2) The choice of the size and shape of the spatial context around each pixel vector should not be a critical parameter requiring fine-tuning; ideally, a spatial–spectral endmember extraction algorithm should effectively behave with different spatial window shapes and sizes.
- 3) Finally, it is highly desirable that the integration of spatial and spectral information does not require significant modifications in the implementation of available endmember extraction algorithms, which are, in most cases, fully automated.

With the preceding features in mind, we develop a novel framework for the integration of spatial and spectral information in the process of endmember extraction. The proposed approach is presented as a preprocessing module that can be used in combination with available spectral-based endmember extraction algorithms. Prior to addressing our approach, let us first categorize four types of pixels (vectors) that can be found

in a hyperspectral scene, along the lines of the definitions given in [25]. A *pure* pixel is a pixel that is made up of a single spectral signature, as opposed to a *mixed* pixel, whose associated spectral signature consists of several different underlying material substances. On the other hand, a *homogeneous* pixel is a pixel whose spectral signature is similar to the signatures of its surrounding pixels and can be considered as the opposite of an *anomalous* pixel, whose signature is spectrally distinct from the signatures of its neighboring pixels. It should be noted that homogeneous and anomalous pixels may or may not be pure.

When searching for image endmembers, it is possible to exploit the spatial similarity between adjacent pixels by defining a criterion that is sensitive to the nature of both *homogeneous* and *transition* areas between different land-cover classes. Intuitively, the transition areas between two or more different land-cover types would likely contain some mixed pixels. Conversely, by definition, an endmember is an idealized pure signature for a class [25]. Thus, it would be reasonable to assume that pure pixels are less likely to be found in such transition areas. In other words, if we assume that homogeneous areas provide good candidate pixel vectors for endmember extraction algorithms, then it is also possible to use the spatial information to intelligently direct the spectral-based endmember search process to these spatially homogeneous regions. In order to accomplish this goal, our approach relies on the introduction of a spatially based pixel similarity metric, which is used to weigh the spectral signature associated to each pixel vector in the scene according to its spatial context.

The remainder of this paper is organized as follows: Section II formulates and describes the proposed preprocessing method, including a geometric interpretation. Implementation details and potential limitations of the proposed method are also discussed. Section III describes the simulated and real hyperspectral data sets used for evaluation purposes and briefly reviews three spectral-based endmember extraction algorithms that will be used in this work in conjunction with the proposed preprocessing module to substantiate its advantages. Experimental results analyzing the performance of the considered endmember extraction algorithms with and without the proposed preprocessing method are discussed in Section IV. Section V concludes with some remarks and a description of future research avenues.

II. METHODOLOGY

A. Problem Formulation

Let us assume that a remotely sensed hyperspectral scene with n bands is denoted by \mathbf{I} , in which the pixel at the discrete spatial coordinates (i, j) of the scene is represented by a vector $\mathbf{X}(i, j) = [x_1(i, j), x_2(i, j), \dots, x_n(i, j)] \in \mathbb{R}^n$, where \mathbb{R} denotes the set of real numbers in which the pixel’s spectral response $x_k(i, j)$ at sensor channels $k = 1, \dots, n$ is included. Under the linear mixture model assumption, each pixel vector in the original scene can be modeled using the following expression:

$$\mathbf{X}(i, j) = \sum_{z=1}^p \Phi_z(i, j) \cdot \mathbf{E}_z + \mathbf{n}(i, j) \quad (1)$$

where \mathbf{E}_z denotes the spectral response of endmember z , $\Phi_z(i, j)$ is a scalar value designating the fractional abundance of endmember z at pixel $\mathbf{X}(i, j)$, p is the total number of endmembers, and $\mathbf{n}(i, j)$ is a noise vector. The solution of the linear spectral mixture problem described in (1) relies on a successful estimation of the number of endmembers p that are present in the input hyperspectral scene \mathbf{I} and also on the correct determination of a set $\{\mathbf{E}_z\}_{z=1}^p$ of endmembers and their correspondent abundance fractions $\{\Phi_z(i, j)\}_{z=1}^p$ at each pixel $\mathbf{X}(i, j)$. Two physical constraints are generally imposed into the model described in (1): 1) abundance nonnegativity constraint (ANC), i.e., $\Phi_z(i, j) \geq 0$, and 2) abundance sum-to-one constraint (ASC), i.e., $\sum_{z=1}^p \Phi_z(i, j) = 1$ [26].

In addition, we assume that the input data set \mathbf{I} contains homogeneous regions with pure pixels; therefore, a search procedure aimed at finding the most spectrally pure signatures in the input scene is feasible. In this case, the final set of image-derived endmembers is denoted by $\Omega = (\mathbf{E}_1, \dots, \mathbf{E}_p) \subset \mathbf{I}$. Several endmember extraction algorithms have been designed to search for endmembers in a hyperspectral scene under the pure pixel assumption previously described (some of these will briefly be reviewed in Section III-A), but most of them do not make use of spatial information.

We propose a novel preprocessing technique that can incorporate spatial information into the process of automatically selecting spectral endmembers. The main idea behind our preprocessing framework is to estimate, for each input pixel vector, a scalar factor $\rho(i, j)$, which is intimately related to the spatial similarity between the pixel and its spatial neighbors, and then to use this scalar factor to spatially weigh the spectral information associated to the pixel. In order to define this procedure in mathematical terms, let us first consider a square-shaped spatial region with a size of $ws \times ws$ pixels that is centered at pixel $\mathbf{X}(i, j)$. In this case, we assume that ws is an odd number and that the processing window has a radius of $d = (ws - 1)/2$ pixels. These values define the neighborhood region that will be considered around each pixel under analysis. With the preceding assumptions in mind, we can define a scalar weight $\alpha(i, j)$ as follows:

$$\alpha(i, j) = \sum_{r=i-d}^{i+d} \sum_{s=j-d}^{j+d} \beta(r-i, s-j) \cdot \gamma(r-i, s-j) \quad (2)$$

with

$$\gamma(r-i, s-j) = \gamma(\mathbf{X}(r, s), \mathbf{X}(i, j)) \quad (3)$$

where γ refers to a similarity measure calculated between the central pixel $\mathbf{X}(i, j)$ and a neighboring pixel $\mathbf{X}(r, s)$. The value resulting from this measure of similarity is weighed by β , which is a scalar value that allows us to assign a different weight to the values of γ calculated inside the region delimited by the window with a size of $ws \times ws$ pixels. In particular, this approach allows us to give more importance to pixels that are spatially adjacent to the central pixel in the window, thus reducing the weight associated to the values of γ calculated for

pixels that are more spatially distant from such central pixel. With this approach, we obtain two main advantages.

- 1) For large values of ws , the weight associated to pixel vectors that are more spatially distant from the central pixel in each $(ws \times ws)$ -pixel neighborhood is decreased, thus preventing the proposed framework from being extremely sensitive to the values of ws defined *a priori* by the user.
- 2) For small values of ws , the lack of information about pixels that are outside the $(ws \times ws)$ -pixel neighborhood is not very critical since the weight associated to pixels in close spatial vicinity of the central pixel of the window is higher than the weight associated to other pixels that could have eventually been encompassed by a larger spatial window.

With the previous rationale in mind, we define a per-pixel spatially derived weighing factor for endmember extraction by the following quadratic expression:

$$\rho(i, j) = \left(1 + \sqrt{\alpha(i, j)}\right)^2. \quad (4)$$

From (4), it turns out that $\rho(i, j) \geq 1$, which places constraints on β and γ in (2). An easy way to guarantee the nonnegativity of $\alpha(i, j)$ in (4) is to require both β and γ to be nonnegative. As will be shown here, these requirements are fulfilled in our proposed formulation. The preceding expression can simply be used to scale the spectral response of an original image pixel as follows:

$$\mathbf{X}(i, j)' = \frac{1}{\rho(i, j)} (\mathbf{X}(i, j) - \bar{\mathbf{I}}) + \bar{\mathbf{I}} \quad (5)$$

where the term $\mathbf{X}(i, j)'$ denotes a spectral signature obtained after weighing $\mathbf{X}(i, j)$ using spatial information, and $\bar{\mathbf{I}}$ is the centroid of the data cloud, which was computed as the mean of all the pixel vectors in the original hyperspectral scene \mathbf{I} .

B. Geometric Interpretation

A simple geometric interpretation of the weighing factor described in (5) is shown in Fig. 1 and is given as a toy example in which only two spectral bands of an input hyperspectral scene are represented against each other for visualization purposes. The idea behind our preprocessing framework is to center each spectral feature in the data cloud around its mean value and then shift each feature straight toward the centroid of the data cloud (which is denoted by O' in Fig. 1) using a spatial-spectral factor given by (4). The shift of each spectral feature in the data cloud is proportional to a similarity measure calculated using both the spatial neighborhood around the pixel under consideration and the spectral information associated to the pixel but without averaging the spectral signature of the pixel. The correction is performed, so that pixels located in spatially homogenous areas (such as the pixel vector labeled "1" in Fig. 1) are expected to have a smaller displacement with regard to their original location in the data cloud than pure pixels surrounded by spectrally distinct substances (e.g., the pixel vectors labeled "2" and "3" in Fig. 1). Resulting from the aforementioned operation, a modified simplex is formed, using not only spectral but also spatial information. It should be noted

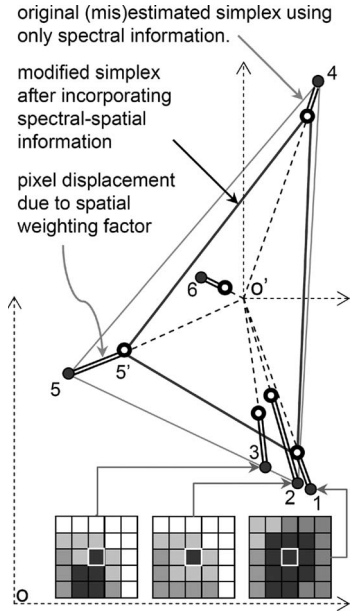


Fig. 1. Geometric interpretation of the proposed preprocessing method.

that the vertices of the modified simplex are more likely to be pure pixels located in spatially homogenous areas. Although the proposed method is expected to privilege homogeneous areas for the selection of endmembers, no pixel is excluded from the competitive endmember extraction process following the preprocessing. As can be inferred from Fig. 1, the proposed method is also expected to be robust in the presence of outliers.

It is important to notice that the modified simplex in Fig. 1 is mainly intended to serve as a guide for a subsequent competitive endmember extraction process, which is conducted using a user-defined algorithm. However, such modified simplex is not intended to replace the simplex in the input hyperspectral scene. To achieve this, the spatial coordinates of the endmembers extracted from the preprocessed image are retained, but the spectral signatures associated to those spatial coordinates are obtained from the original hyperspectral scene. This approach is shown in Fig. 2, which provides a flowchart of the preprocessing technique in combination with a certain endmember extraction and spectral unmixing algorithm. As shown in Fig. 2, the estimation of the number of endmembers is conducted using the original hyperspectral image as input. On the other hand, the modified hyperspectral image resulting from our spatial preprocessing is only used as input to the endmember extraction algorithm. The spatial coordinates of extracted endmembers are retained and used to form a final set Ω , which comprises the original image pixels at such coordinates. Then, a spectral unmixing process is conducted using the original hyperspectral image and the set Ω as inputs. As a result, no artifacts are introduced in the process of estimating abundance fractions.

To conclude this section, we emphasize that the general flowchart shown in Fig. 2 can be used in combination with different techniques for endmember extraction and spectral unmixing. In addition, the factor described in (4) can be defined using different measures for the spectral similarity criterion γ and the spatial weight function β defined in (2). In the next section, we describe our empirical choices for both parameters in this paper.

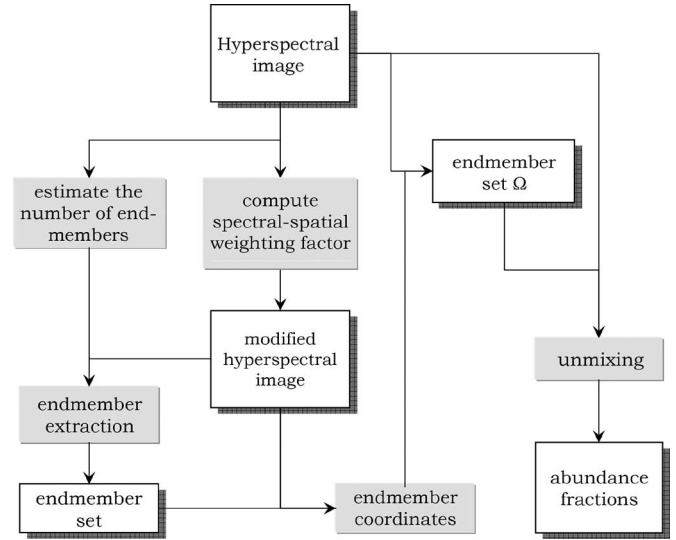


Fig. 2. Flowchart of the proposed method for incorporating spatial-spectral information into the endmember extraction and unmixing process.

C. Spectral Similarity Measures and Spatial Neighborhood Weight

Several pointwise distances can be considered in order to compute the spectral similarity metric γ used in (4). In this paper, we have used the SAD, which is a well-known metric for hyperspectral data processing [4]. SAD can be used to measure the spectral similarity between two pixel vectors $\mathbf{X}(i, j)$ and $\mathbf{X}(r, s)$ as follows:

$$\gamma = \text{SAD}(\mathbf{X}(i, j), \mathbf{X}(r, s)) = \cos^{-1} \frac{\mathbf{X}(i, j) \cdot \mathbf{X}(r, s)}{\|\mathbf{X}(i, j)\| \|\mathbf{X}(r, s)\|}. \quad (6)$$

It should be noted that SAD is given by the spectral angle formed by n -dimensional vectors (in radians). As a result, low SAD scores mean high spectral similarity between the compared vectors. This spectral similarity measure is invariant in the multiplication of $\mathbf{X}(i, j)$ and $\mathbf{X}(r, s)$ by constants and, consequently, is invariant before unknown multiplicative scalings that may arise due to differences in illumination and angular orientation [6]. In addition, this similarity measure satisfies the following properties: 1) $\text{SAD}(\mathbf{X}(i, j), \mathbf{X}(r, s)) \geq 0$, with 2) equality if and only if $\mathbf{X}(i, j) = \mathbf{X}(r, s)$, and 3) $\text{SAD}(\mathbf{X}(i, j), \mathbf{X}(r, s)) = \text{SAD}(\mathbf{X}(r, s), \mathbf{X}(i, j))$.

On the other hand, spatial weight function β (excluding the central pixel) is taken as proportional to the quadratic distance of each pixel inside region ws and the central pixel, which is normalized to sum to 1, i.e.,

$$\beta(i, j) \propto \frac{1}{(i^2 + j^2)}. \quad (7)$$

Thus, the SAD spectral similarity score obtained after comparing the spectral signature associated to the central pixel with that of its spatial neighbors receives more importance than the scores obtained after comparing the same pixel with more distant neighbors. Notice that β and γ guarantee the positivity of α in (4). At this point, $\rho(i, j) \geq 1$ is verified, with equality if and only if all the spectra in the window are identical. This follows

from properties 1 and 2, and the fact that the values of β are nonnegative and that their sum is strictly positive. By applying (6) and (7), it is easy to deduce that, regardless of the size of the considered window, the spatial-derived weighing factor defined in (4) is bounded by values $1 \leq \rho(i, j) \leq 4$ if the values of γ in (6) are scaled to lie in the range $[0, 1]$. The justification for using (4), instead of other possible formulations, such as $\rho(i, j) = 1 + \alpha(i, j)$, is that, usually, $\alpha(i, j)$ is a small value (lower than 1), so this value is increased by the square root. The alternative formulation would lead to less displacement in the simplex vertices.

D. Known Limitations of the Proposed Method

Before concluding our presentation of the proposed methodology, it is important to emphasize that, as a new approach, there are some unresolved issues that may present challenges over time. It is important to note that our preprocessing framework will penalize the selection of anomalous pixels and increase the probability that an endmember extraction algorithm applied after the preprocessing ends up selecting the majority of pixels that are homogeneous in nature. As a result, we expect the proposed approach to be less effective in specific tasks, such as detection of *small* targets or anomalous areas. Although these areas are not theoretically excluded after the preprocessing, such regions would be more penalized by our proposed spatial-spectral homogeneity criteria. It is also worth noting that, in any event, the term *small* in the previous sentence relates to the size *ws* of a processing window that can be controlled and defined in advance by the end user and to the size of such window in comparison with observed objects.

As an additional remark, it is important to note that a possible solution in overcoming the possible loss of anomalous endmembers could be the definition of a second filter that looks for single pixels that are distinct from their surroundings, with both homogeneous (the current implementation) and anomalous regions having increased weight in the search for endmembers. This solution is listed as one of the topics deserving future research in this area.

III. EXPERIMENTAL SETUP

This section describes the setup for an experimental evaluation, with the ultimate goal of assessing the impact of the proposed preprocessing technique on endmember extraction and spectral unmixing. The section is organized as follows: First, we describe the endmember extraction algorithms selected for experiments in this paper. These algorithms have been implemented in the Matlab environment, with the OSP and N-FINDR written in house and vertex component analysis (VCA) provided by the authors of the algorithm. Then, we describe the simulated and real hyperspectral data sets used for evaluation purposes in the next section.

A. Endmember Extraction Algorithms

While the selection of algorithms for performance comparison is subjective, it is our desire to make our selection as representative as possible. For that purpose, three well-known

endmember extraction algorithms have been selected for our comparative study, including the N-FINDR algorithm in [10], the VCA algorithm in [27], and the OSP algorithm in [14]. The reasons for our selection are given as follows: 1) these algorithms are representative of a class of convex geometry-based techniques that have been successful in endmember extraction; 2) they are fully automated; 3) they always produce the same final results for the same input parameters; and 4) they do not require any input parameters other than the number of endmembers p to be detected by each method. We believe that the three considered algorithms are sufficient to illustrate the advantages of the proposed spatial-spectral framework when the same set of algorithms is used with and without the proposed preprocessing technique. Before briefly reviewing our selected algorithms, we emphasize that the recently developed concept of virtual dimensionality (VD) [4] was used in this work to estimate p , i.e., the number of endmembers to be extracted. Despite the fact that the VD may not necessarily correspond to the intrinsic dimensionality of the data, it has been shown in the literature that this criterion is useful in practice, because it can provide a good estimate of the number of spectrally distinct signatures that characterize the given data set. The VD concept formulates the issue of whether a distinct signature is present or not in each of the spectral bands as a binary hypothesis testing problem, where a so-called Neyman-Pearson detector is generated to serve as a decision maker based on a prescribed P_F (i.e., false alarm probability). In light of this interpretation, the issue of determining an appropriate value for p is further simplified and reduced to setting a specific value of P_F . As will be shown in experiments, a suitable empirical choice is $P_F = 10^{-3}$ or $P_F = 10^{-4}$, where the method used in this work to estimate the VD is the one developed by Chang [4] (referred to as the Harsanyi-Farrand-Chang (HFC) method), which was later modified by including a noise-whitening process as preprocessing to remove the second-order statistical correlation. The purpose is that signal sources can be decorrelated from the noise to achieve better signal detection. The resulting method will be referred to as the noise-whitened HFC (NWHFC).

1) *N-FINDR*: This algorithm looks for the set of pixels with the largest possible volume by *inflating* a simplex inside the data. The procedure begins with a random initial selection of pixels. Every pixel in the image must be evaluated in order to refine the estimate of endmembers, looking for the set of pixels that maximizes the volume of the simplex defined by selected endmembers. The volume of the simplex is calculated with every pixel in place of each endmember. The corresponding volume is calculated for every pixel in each endmember position by replacing that endmember and finding the resulting volume. If the replacement results in an increase in volume, the pixel replaces the endmember. This procedure is repeated until there are no more endmember replacements. The mathematical definition of the volume of a simplex formed by a set of endmember candidates Ω is proportional to the determinant of the set augmented by a row of ones. The determinant is only defined in the case where the number of features is $p - 1$, with p being the number of desired endmembers [5]. Since, in hyperspectral data, typically $n \gg p$, a transformation that reduces the dimensionality of the input data is required. In this work,

the principal component transform has been used, although another widely used alternative that decorrelates the noise in the data is the maximum noise fraction [28]. As a final comment, it has been observed that different random initializations of N-FINDR may produce different final solutions. Thus, our N-FINDR algorithm was implemented in iterative fashion, so that each sequential run was initialized with the previous algorithm solution, until the algorithm converges to a simplex volume that cannot further be maximized. Our experiments show that, in practice, this approach allows the algorithm to converge in a few iterations only.

2) *OSP*: This algorithm starts by selecting the pixel vector with maximum length in the scene as the first endmember. Then, it looks for the pixel vector with the maximum absolute projection in the space orthogonal to the space linearly spanned by the initial pixel and labels that pixel as the second endmember. A third endmember is found by applying an orthogonal subspace projector to the original image, where the signature that has the maximum orthogonal projection in the space orthogonal to the space linearly spanned by the first two endmembers. This procedure is repeated until the desired number of endmembers p is found.

3) *VCA*: This algorithm also makes use of the concept of OSPs. However, as opposed to the OSP algorithm previously described, the VCA exploits the fact that the endmembers are the vertices of a simplex and that the affine transformation of a simplex is also a simplex [27]. As a result, VCA models the data using a positive cone, whose projection onto a properly chosen hyperplane is another simplex whose vertices are the final endmembers. After projecting the data onto the selected hyperplane, the VCA projects all image pixels to a random direction and uses the pixel with the largest projection as the first endmember. The other endmembers are identified in sequence by iteratively projecting the data onto a direction orthogonal to the subspace spanned by the endmembers already determined. The new endmember is then selected as the pixel corresponding to the extreme projection, and the procedure is repeated until a set of p endmembers is found [27]. In our experiments with VCA, we select the corresponding pixel original spectra as the VCA solution and not the noise-smoothed solution produced by the original algorithm. In practice, our approach is expected to slightly reduce the performance of VCA for low signal-to-noise (SNR) ratios, but we also believe that this decision allows a fair comparison of VCA to N-FINDR and OSP, which do not incorporate such noise reduction stage.

B. Synthetic Hyperspectral Data Sets

Our primary reason for using simulated imagery as a complement to real data analysis is that all the details of the simulated images are known in advance. These details can efficiently be investigated, because they can individually and precisely be manipulated. As a result, algorithm performance can be examined in a controlled manner. Specifically, we have generated two distinct spatial patterns, which are then used to simulate linear mixtures of reflectance signatures selected from a spectral library compiled by the U.S. Geological Survey

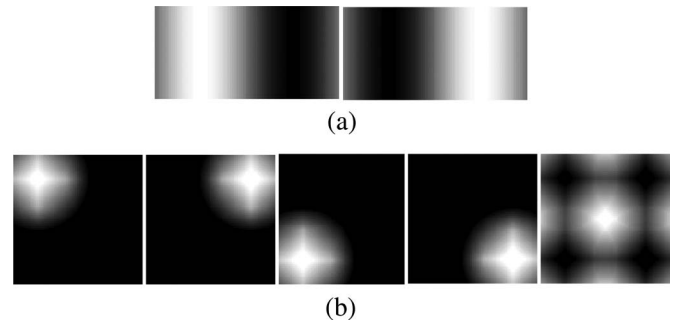


Fig. 3. Synthetic data sets used for experiments. (a) Abundance fractions for spectral signatures (left) S_1 and (right) S_2 in simulated scene DS01. (b) (Left to right) Abundance fractions for spectral signatures S_1, \dots, S_5 in simulated scene DS02. (Black) 0% abundance. (White) 100% abundance.

(USGS).¹ The reflectance spectra of 22 USGS ground mineral spectra (including, among others, alunite, buddingtonite, calcite, kaolinite, muscovite, chlorite, jarosite, montmorillonite, nontronite, and pyrophyllite), which were convolved to AVIRIS wavelengths and selected due to their known presence in the AVIRIS Cuprite image² that will be used later on in real data experiments, have been managed in computer simulations to generate two synthetic data cubes comprising distinct spatial patterns, where the ground-truth fractional abundance maps for those scenes are shown in Fig. 3(a) and (b), respectively. The synthetic data sets were generated as follows:

1) *DS01*: This scene, with a size of 100×50 pixels, simulates a spatial pattern in which the abundances of two spectral signatures designated by S_1 and S_2 are assigned using a spatial-sinusoidal shape, in which their abundances are defined by equations $\Phi_1(i, j) = (1/2)(1 + \sin(\xi))$ and $\Phi_2(i, j) = (1/2)(1 - \sin(\xi))$, respectively, with $\xi = 0 + (2\pi/99)(j - 1)$. In both cases, $j = 1, \dots, 100$ represents the image rows, and $i = 1, \dots, 50$ represents the image columns. All the pixels in the same column share the same fractional abundances, as shown in Fig. 3(a).

2) *DS02*: This scene, with a total final size of 80×80 pixels, was created by using five spectral signatures, i.e., S_1, S_2, S_3 , and S_4 (which were arranged at the corners of the image) and S_5 (which was arranged at the center of the image). The scene was simulated, so that signature abundance decreases linearly away from the specified points (from 100% to 0% abundance) being the radius of the resulting circles of 32 pixels in size. In order to avoid the presence of pure pixels at the corner of the simulated scene, a mirroring technique was applied to the image borders to replicate such borders in symmetric fashion, thus obtaining the spatial abundance patterns that are shown in Fig. 3(b). The spectral signatures used to simulate the two synthetic scenes previously described were randomly selected from the 22 mineral ground spectra taken from the USGS library.

Zero-mean Gaussian noise was finally added (in different SNR proportions, from 10 : 1 to 300 : 1) to the two aforementioned scenes to simulate contributions from ambient (clutter) and instrumental sources, following the procedure described in [13]. Here, the SNR is defined as the ratio of the mean signal to the standard deviation of the noise.

¹<http://speclab.cr.usgs.gov/spectral-lib.htm>

²<http://speclab.cr.usgs.gov/PAPERS/tetracorder/>



Fig. 4. (a) False color composition of the AVIRIS Indian Pines scene. (b) Ground-truth map containing 16 mutually exclusive land-cover classes.

C. Real Hyperspectral Data Sets

1) *AVIRIS Indian Pines Scene*: This scene, with a size of 145×145 pixels, was acquired by the AVIRIS sensor in June 1992 over the Indian Pines area in northwestern Indiana, which is a mixed agricultural/forest area, early in the growing season. The scene comprises 220 spectral channels in the wavelength range of $0.4\text{--}2.5 \mu\text{m}$. After an initial screening, several spectral bands were removed from the data set due to noise and water absorption phenomena, leaving a total of 190 radiance channels to be used in the experiments. For illustrative purposes, Fig. 4(a) shows a false color composition of the AVIRIS Indian Pines scene, whereas Fig. 4(b) shows the ground-truth map available for the scene, which is displayed in the form of a class assignment for each labeled pixel, with 16 mutually exclusive ground-truth classes. These data, including ground truth, are available online,³ which is a fact that has made this scene a widely used benchmark for testing the accuracy of hyperspectral data classification algorithms. Unfortunately, no ground-truth information about the location of pure pixels and/or the true fractional abundances of endmembers is available for this scene (as it is often the case in most real-world applications). Despite the lack of ground truth at subpixel levels, an alternative strategy will be used in this work to validate the quality of extracted endmembers using available labeled pixels, as will be described in Section IV-B.

2) *AVIRIS Cuprite Scene*: The second real scene used in experiments is the well-known AVIRIS Cuprite data set, which is available online in reflectance units⁴ after atmospheric correction. This scene has widely been used to validate the performance of endmember extraction algorithms. The portion used in experiments corresponds to a subset of the sector with 250×200 pixels that is labeled as f970619t01p02_r02_sc03.a.rf1 in the online data. The scene comprises 224 spectral bands be-

tween 0.4 and $2.5 \mu\text{m}$, with a full-width at half-maximum of 10 nm . Prior to the analysis, several bands were removed due to water absorption and low SNR in those bands, leaving a total of 192 reflectance channels to be used in the experiments. The Cuprite site is mineralogically well understood [29], [30] and has several exposed minerals of interest, including those used in the USGS library considered for the generation of simulated data sets. These laboratory spectra, which were convolved in accordance with AVIRIS wavelength specifications, will be used to assess endmember signature purity in this work. At this point, it is important to note that many of the mineral spectra in the USGS library are not from the Cuprite area. Thus, the best match between an image endmember and one in the USGS library spectra does not necessarily mean the best match with the Cuprite endmember. In addition, some minerals do not occur in pure form in the area (specifically at the 20-m spatial resolution of the sensor).

IV. COMPARATIVE PERFORMANCE ANALYSIS

This section describes a set of experiments that use both simulated and real hyperspectral data to conduct a comprehensive analysis of the proposed preprocessing method when combined with standard endmember extraction algorithms. For that purpose, we test the same set of algorithms with and without spatial preprocessing. As a result, the effect of using the proposed preprocessing can be isolated and substantiated.

In order to ensure the fairest possible comparison, the best performance must be obtained from each alternative method. Then, prior to a full examination and discussion of results, it is important to outline parameter values used for endmember extraction algorithms. The fact that the only input parameter to the three selected algorithms is p , which is the number of endmembers to be detected by each method, allows us to separately investigate the impact of the proposed preprocessing module from other distinct algorithm features. On the other hand, the only input parameter of our preprocessing (window size ws) will carefully be analyzed in the following experiments.

³<http://aviris.jpl.nasa.gov/html/aviris.freedata.html>

⁴<http://aviris.jpl.nasa.gov/html/aviris.freedata.html>

A. Experiment 1: Synthetic Hyperspectral Data Sets

In this section, we conduct an experiment-based evaluation of our proposed spatial preprocessing framework using the two simulated scenes DS01 and DS02 with different SNR values. In particular, we focus on evaluating the performance of a hyperspectral data-processing chain made up of the following steps: spatial preprocessing (optional), endmember extraction (N-FINDR, OSP, and VCA), and fully constrained linear spectral unmixing (FCLSU) that performs a least-squares fitting of (1) with the ANC and ASC constraints [26]. The number of endmembers to be extracted from the simulated scenes was fixed (to $p = 2$ in DS01 and $p = 5$ in DS02) based on prior knowledge. In order to better quantify our findings, each run of the aforementioned full data-processing chain was repeated 25 times, each time using a distinct simulated hyperspectral data set with the same abundance fractions shown in Fig. 3, but with a random choice of endmembers (without repetitions in the same scene) randomly obtained from the 22 USGS spectral signatures.

Two different metrics have been used to compare the performance of the aforementioned data-processing chain, with and without spatial preprocessing. The first metric is the SAD between each extracted endmember and the set of available USGS ground-truth spectral signatures. This allows us to identify the USGS signature, which is most similar to each endmember automatically extracted from the scene by observing the minimum SAD distance reported for such endmember across the entire set of USGS signatures. A second metric has also been used based on the assumption that, in the simulated images, the abundance fractions of each endmember are known on a per-pixel basis. In order to define this metric, let s be the total number of columns and l be the total number of rows in the simulated hyperspectral image. In addition, let \mathbf{E}_k be an endmember extracted from the simulated image and \mathbf{S}_k be the spectral signature in the USGS library, which is most similar to endmember \mathbf{E}_k . Similarly, let $\hat{\Phi}_k(i, j)$ denote the FCLSU-estimated abundance of \mathbf{E}_k at the pixel with spatial coordinates (i, j) , with $\Phi_k(i, j)$ being the true abundance of \mathbf{S}_k at the same pixel. A simple statistical measurement to evaluate the similarity of true versus estimated fractional abundances is the root mean square error (RMSE) between the true and FCLSU-estimated fractional abundances associated to a certain endmember \mathbf{E}_k , which is given by

$$\text{RMSE}(\mathbf{E}_k, \mathbf{S}_k) = \left(\frac{1}{s \times l} \sum_{i=1}^s \sum_{j=1}^l \left(\Phi_k(i, j) - \hat{\Phi}_k(i, j) \right)^2 \right)^{\frac{1}{2}}. \quad (8)$$

With the preceding expression in mind, an average RMSE score can be calculated as follows:

$$\text{RMSE} = \frac{1}{p} \sum_{k=1}^p \text{RMSE}(\mathbf{E}_k, \mathbf{S}_k). \quad (9)$$

For illustrative purposes, Fig. 5(a) shows the SAD-based spectral similarity scores between extracted endmembers and ground-truth signatures in simulated scene DS01, whereas Fig. 5(b) shows the RMSE-based similarity scores between

estimated and true fractional abundances in the same simulated scene. On the other hand, Fig. 5(c) and (d) shows the same results for simulated scene DS02, respectively. We emphasize that each bar result given in Fig. 5 corresponds to the average of 25 runs. The figures report the results for N-FINDR (green color in the figure), OSP (red), and VCA (blue), without spatial preprocessing (shown in the figure as $ws = 0$) and with spatial preprocessing, using different window sizes, i.e., from $ws = 3$ to $ws = 11$. In all cases, the SAD- and RMSE-based results are multiplied by a constant scalar value (100) to facilitate the representation.

As shown in Fig. 5, the three compared algorithms provided endmembers that resulted in lower SAD-based scores when spatial preprocessing was used, compared with those obtained without spatial preprocessing for both DS01 [see Fig. 5(a)] and DS02 [see Fig. 5(c)]. A similar observation can be made for RMSE-based scores for both DS01 and DS02. As expected, as SNR increases, the SAD- and RMSE-based error scores significantly decrease. An interesting observation, however, can be made for simulated scene DS02 with a very low SNR of 10 : 1. In this case, we observed that the OSP algorithm did not seem to benefit from the spatial preprocessing, resulting in high SAD- and RMSE-based error scores. This effect may be attributed to the higher complexity of simulated scene DS02, which contains ternary mixtures in addition to binary mixtures. However, a similar effect on RMSE was also observed for the same OSP algorithm when applied to simulated scene DS01 with an SNR of 30 : 1 [see Fig. 5(b)]. Although the SNR values of 10 : 1 and 30 : 1 previously reported are very low in comparison to those routinely achieved in the design of state-of-the-art imaging spectrometers, such as AVIRIS [2], our experiments reveal that additional attention must be taken when using the proposed method to process significantly noise-degraded images.

Overall, the results in Fig. 5 suggest that the incorporation of spatial information prior to endmember extraction can be beneficial since a clear pattern of improvement on both SAD- and RMSE-based error scores was observed for all the considered algorithms. In addition, the results reported are not very sensitive to the size ws of the preprocessing window, which seems to be a positive aspect for the practical use of the method. This is mainly due to the quadratic square-based distance weighing strategy implemented by (7). Fig. 6 shows an example of the behavior of the spatial weighing factor ρ when applied to all the pixels in one of the randomly generated versions of simulated data set DS02 (with an SNR of 50 : 1), considering three window sizes of $ws = 3$, $ws = 5$, and $ws = 11$.

In an attempt to explain the significance of the obtained results, we also have conducted a simple statistical analysis of the accuracy of results shown in Fig. 5. Specifically, the paired differences between the accuracies obtained using the endmember extraction algorithms with and without spatial preprocessing have been compared using a test of statistical significance based on the randomization reference distribution [31]. Let us consider the hypothesis that the accuracies obtained using spatial preprocessing ($ws > 0$) and those obtained without using such preprocessing ($ws = 0$) are the same. If we assume that this hypothesis is true, then the differences measured for each distinct run (which results in a pair of accuracy results)

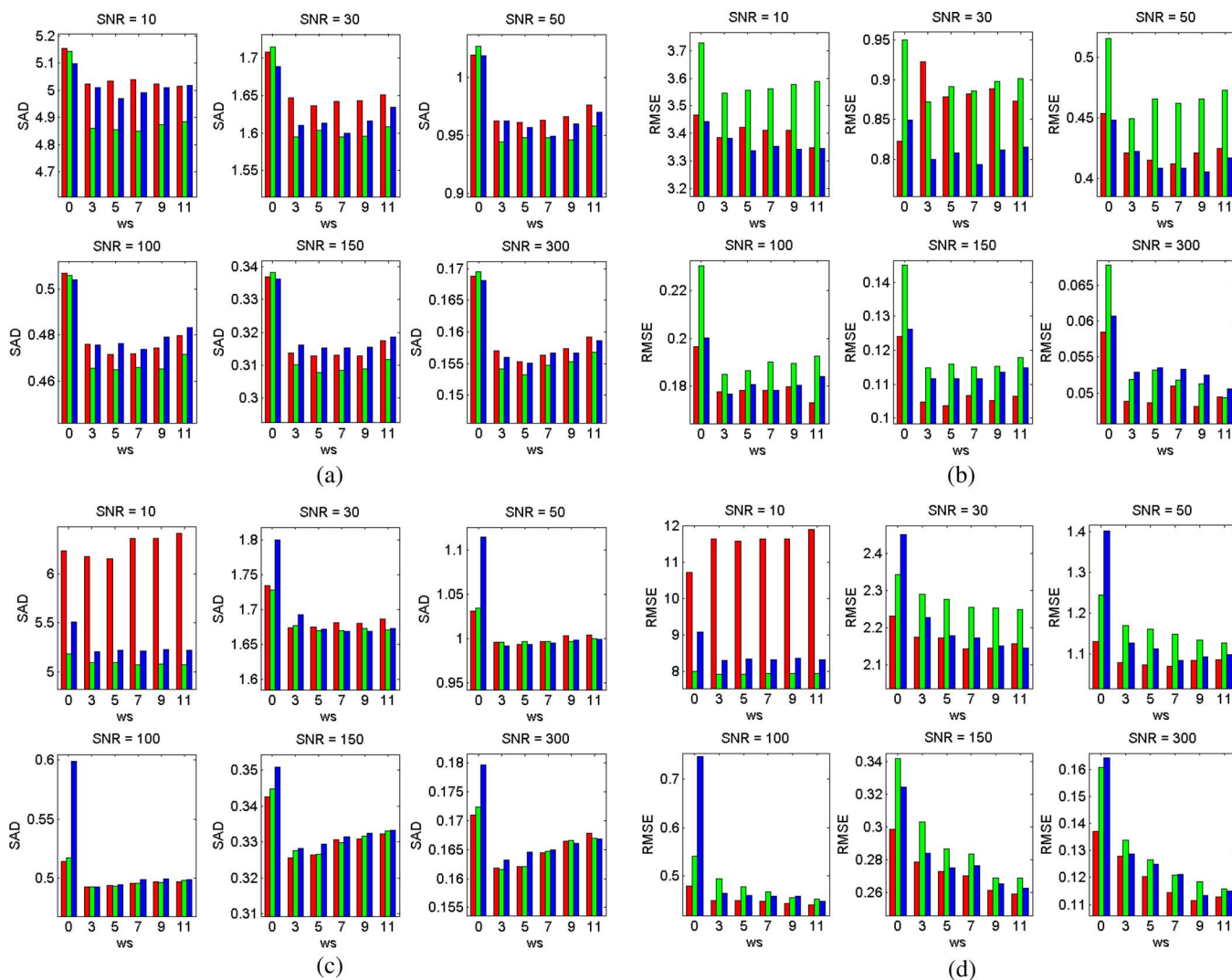


Fig. 5. (a) SAD-based spectral similarity scores between extracted endmembers and ground-truth USGS signatures in the first simulated scene DS01. (b) RMSE-based similarity scores between FCLSU-estimated and ground-truth abundance fractions in the first simulated scene DS01. (c) SAD-based spectral similarity scores between extracted endmembers and ground-truth USGS signatures in the second simulated scene DS02. (d) RMSE-based similarity scores between FCLSU-estimated and ground-truth abundance fractions in the second simulated scene DS02. Three different endmember extraction algorithms are compared: (green) N-FINDR, (red) OSP, and (blue) VCA. In all cases, $ws = 0$ indicates no spatial preprocessing, and $ws > 0$ indicates spatial preprocessing (prior to endmember extraction) using different window sizes.

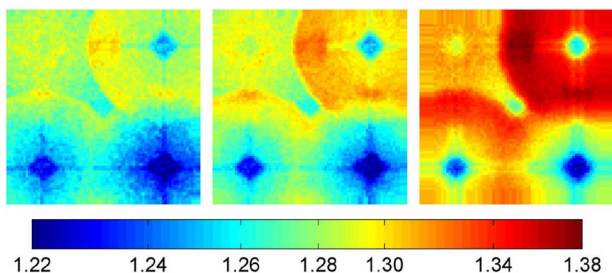


Fig. 6. Spatial representation of the weighing factor ρ calculated for one of the randomly generated versions of simulated scene DS02 (with an SNR of 50:1), using spatial window sizes of (left) $ws = 3$, (middle) $ws = 5$, and (right) $ws = 11$.

should not be related to their individual values and merely affect the sign associated with those differences. With this assumption in mind, the sequence of sign differences observed for the 25 runs is therefore one of 2^{25} equiprobable outcomes. To test the aforementioned hypothesis, the average difference \bar{d}

actually observed and shown in Fig. 5 may be compared with the other 2^{25} average differences that could have resulted from different random outcomes. The complete set of 2^{25} differences is obtained by averaging the 25 differences with all possible combinations of plus and minus signs. Thus, the probability $p_{\bar{d}}$ for the actual value indicates the number of times that the differences produced by the randomization process provide values of differences greater than the actual value. Specifically, our statistical significance test (summarized in Table I) has been computed, including 10 000 of such randomizations. From Table I, it can be observed that, for most of the considered algorithms and SNR values, the actual difference is quite unusual (in many cases, $p_{\bar{d}} < 1\%$), which indicates that the randomization test revealed a statistically significant decrease in the estimation errors, which can directly be related to the application of our proposed spatial preprocessing method.

A more detailed evaluation of the overall performance of the proposed preprocessing method is shown in Tables II

TABLE I
STATISTICAL SIGNIFICANCE LEVELS (IN PERCENTAGE) FOR SAD- AND RMSE-BASED ERROR SCORES (IN PARENTHESES) OBTAINED IN EXPERIMENTS WITH SIMULATED HYPERSPECTRAL DATA SETS DS01 AND DS02 AT DIFFERENT SNRS. THESE PERCENTAGES INDICATE THE STATISTICAL SIGNIFICANCE OF THE RESULTS REPORTED, WITH LOW PERCENTAGES (< 1%) MEANING HIGH SIGNIFICANCE AND HIGHER PERCENTAGES INDICATING LOWER SIGNIFICANCE

SNR	Algorithm	DS01					DS02				
		$ws = 3$	$ws = 5$	$ws = 7$	$ws = 9$	$ws = 11$	$ws = 3$	$ws = 5$	$ws = 7$	$ws = 9$	$ws = 11$
10:1	OSP	0.0 (5.6)	0.0 (16.8)	0.0 (13.1)	0.0 (12.2)	0.0 (3.0)	41.4 (80.0)	40.9 (78.8)	56.6 (80.7)	56.7 (80.8)	62.8 (88.3)
10:1	N-FINDR	0.0 (0.0)	0.0 (0.0)	0.0 (0.0)	0.0 (0.0)	0.0 (0.0)	0.0 (4.0)	0.0 (4.2)	0.0 (9.2)	0.0 (4.8)	0.0 (5.8)
10:1	VCA	0.0 (3.7)	0.0 (1.5)	0.0 (2.1)	0.2 (0.6)	0.2 (0.7)	12.3 (3.9)	14.4 (5.2)	12.6 (4.7)	15.0 (5.9)	13.9 (5.3)
30:1	OSP	0.2 (74.9)	0.0 (49.9)	0.1 (49.9)	0.1 (49.9)	0.2 (49.9)	0.0 (6.0)	0.0 (7.3)	0.0 (1.5)	0.0 (2.5)	0.0 (2.0)
30:1	N-FINDR	0.0 (0.0)	0.0 (0.0)	0.0 (0.0)	0.0 (0.0)	0.0 (0.0)	0.0 (1.9)	0.0 (1.1)	0.0 (0.1)	0.0 (0.1)	0.0 (0.1)
30:1	VCA	0.0 (0.0)	0.0 (0.0)	0.0 (0.0)	0.0 (0.0)	0.0 (0.1)	1.9 (25.8)	0.0 (4.2)	0.0 (2.8)	0.0 (0.9)	0.0 (0.7)
50:1	OSP	0.0 (1.5)	0.0 (0.2)	0.0 (0.2)	0.0 (0.4)	0.0 (0.8)	0.0 (1.4)	0.0 (0.6)	0.0 (0.99)	0.0 (1.3)	0.0 (1.7)
50:1	N-FINDR	0.0 (0.0)	0.0 (0.0)	0.0 (0.0)	0.0 (0.0)	0.0 (0.0)	0.0 (0.0)	0.0 (0.0)	0.0 (0.0)	0.0 (0.0)	0.0 (0.0)
50:1	VCA	0.0 (4.5)	0.0 (0.0)	0.0 (0.0)	0.0 (0.0)	0.0 (0.4)	0.0 (5.4)	0.0 (2.1)	0.0 (0.2)	0.0 (0.6)	0.0 (0.8)

TABLE II
NUMBER OF TIMES THAT THE PROPOSED SPATIAL PREPROCESSING METHOD WINS-TIES-LOSES (OUT OF 25 RUNS), WHEN COMPARED WITH THAT WITHOUT SPATIAL PREPROCESSING PRIOR TO ENDMEMBER EXTRACTION FROM SIMULATED SCENE DS01. THE SCORES ARE OBTAINED USING SAD AND RMSE (IN PARENTHESIS)

SNR	Algorithm	$ws = 3$	$ws = 5$	$ws = 9$
10:1	OSP	13-12-0 (9-12-4)	13-11-1 (8-11-6)	14-9-2 (8-9-8)
10:1	N-FINDR	20-4-1 (18-4-3)	20-5-0 (17-5-3)	19-5-1 (18-5-2)
10:1	VCA	11-13-1 (9-13-3)	13-12-0 (10-12-3)	9-16-0 (8-16-1)
30:1	OSP	17-5-3 (16-5-4)	18-6-1 (16-6-3)	18-6-1 (16-6-3)
30:1	N-FINDR	20-4-1 (21-4-0)	19-6-0 (19-6-0)	19-6-0 (19-6-0)
30:1	VCA	19-6-0 (16-6-3)	18-7-0 (15-7-3)	16-8-1 (15-8-2)
50:1	OSP	22-3-0 (15-3-7)	22-3-0 (16-3-6)	19-6-0 (15-6-4)
50:1	N-FINDR	22-2-1 (23-2-0)	22-2-1 (23-2-0)	22-3-0 (22-3-0)
50:1	VCA	18-7-0 (14-7-4)	20-5-0 (19-5-1)	20-3-2 (19-3-3)
300:1	OSP	24-0-1 (21-0-4)	24-0-1 (22-0-3)	21-1-3 (22-1-2)
300:1	N-FINDR	25-0-0 (24-0-1)	25-0-0 (25-0-0)	25-0-0 (24-0-1)
300:1	VCA	22-2-1 (19-2-4)	24-1-0 (20-1-4)	23-1-1 (19-1-5)

TABLE III
NUMBER OF TIMES THAT THE PROPOSED SPATIAL PREPROCESSING METHOD WINS-TIES-LOSES (OUT OF 25 RUNS) WHEN COMPARED WITH THAT WITHOUT SPATIAL PREPROCESSING PRIOR TO ENDMEMBER EXTRACTION FROM SIMULATED SCENE DS02. THE SCORES ARE OBTAINED USING SAD AND RMSE (IN PARENTHESIS)

SNR	Algorithm	$ws = 3$	$ws = 5$	$ws = 9$
10:1	OSP	15-5-5 (9-5-11)	16-4-5 (12-4-9)	14-5-6 (12-5-8)
10:1	N-FINDR	18-4-3 (12-4-9)	18-5-2 (12-5-8)	18-6-1 (10-6-9)
10:1	VCA	18-3-4 (17-3-5)	16-3-6 (16-3-6)	17-3-5 (16-3-6)
30:1	OSP	22-1-2 (15-1-9)	20-1-4 (15-1-9)	19-2-4 (14-2-9)
30:1	N-FINDR	20-2-3 (16-2-7)	21-2-2 (15-2-8)	23-1-1 (18-1-6)
30:1	VCA	20-3-2 (14-3-8)	22-3-0 (15-3-7)	24-1-0 (16-1-8)
50:1	OSP	20-0-5 (17-0-8)	21-1-3 (19-1-5)	20-0-5 (18-0-7)
50:1	N-FINDR	20-2-3 (18-2-5)	23-1-1 (19-1-5)	24-0-1 (21-0-4)
50:1	VCA	23-1-1 (14-1-10)	23-1-1 (15-1-9)	22-1-2 (16-1-8)
300:1	OSP	25-0-0 (18-0-7)	25-0-0 (20-0-5)	19-0-6 (21-0-4)
300:1	N-FINDR	25-0-0 (23-0-2)	24-0-1 (24-0-1)	20-0-5 (24-0-1)
300:1	VCA	25-0-0 (19-0-6)	24-0-1 (18-0-7)	22-0-3 (23-0-2)

and III, which report the number of runs (out of 25) in which the SAD and RMSE scores, respectively, were better than, equal to, and worse than the respective values without using spatial preprocessing. As reported in Tables II and III, preprocessing does not always guarantee better results, but it does frequently produce results that are equal to or better than the results obtained without using spatial preprocessing.

B. Experiment 2: AVIRIS Indian Pines Scene

Our analysis with this real hyperspectral scene begins with the estimation of the number of endmembers p present in the original scene, using the VD concept in [32]. After estimating this value via the NWHFC method (using different values of false alarm probability P_F), a reasonable estimate for the VD was 18 when $P_F = 10^{-3}$ or lower. It should be noted that the spatial

preprocessing stage did not significantly affect the estimation of the number of endmembers in the scene, which is a highly desirable feature. The value $p = 18$ seems reasonable in light of the number of distinct land-cover classes labeled in the ground-truth map displayed in Fig. 4(b). Therefore, only the experiments for a case study with $p = 18$ are discussed in this section.

The only available information *a priori* is a ground-truth map that assigns a (hard) class label to each image pixel, with no further information about subpixel abundance fractions. In this context, our hypothesis is that a set of high-quality endmembers (and their corresponding FCLSU-estimated abundance fractions) may allow reconstruction of the original hyperspectral scene [by means of (1)] with higher precision than a set of low-quality endmembers. In other words, our main goal in experiments with this scene is to analyze the reconstruction error, which can be seen as an indirect assessment of the accuracy of

TABLE IV

INDIVIDUAL AND OVERALL RMSE-BASED RECONSTRUCTION ERRORS OBTAINED AFTER COMPARING THE ORIGINAL AVIRIS INDIAN PINES SCENE WITH A RECONSTRUCTED VERSION OF THE SAME SCENE USING THE FULLY CONSTRAINED LINEAR MIXTURE MODEL IN (1) AND THE ENDMEMBERS EXTRACTED BY OSP, N-FINDR, AND VCA ALGORITHMS. TWO CASES ARE REPORTED FOR EACH ALGORITHM: WITHOUT SPATIAL PREPROCESSING ($ws = 0$) AND WITH SPATIAL PREPROCESSING PRIOR TO ENDMEMBER EXTRACTION, USING WINDOW SIZES OF $ws = 3$, $ws = 5$, AND $ws = 9$

Class (number of pixels)	OSP				N-FINDR				VCA			
	$ws = 0$	$ws = 3$	$ws = 5$	$ws = 9$	$ws = 0$	$ws = 3$	$ws = 5$	$ws = 9$	$ws = 0$	$ws = 3$	$ws = 5$	$ws = 9$
Alfalfa (54)	55.16	45.90	44.99	47.28	33.16	41.53	41.98	37.77	70.18	49.12	37.84	46.34
Corn-notill (1434)	37.76	23.49	25.18	33.89	40.17	26.40	31.85	30.01	35.48	30.49	33.06	31.31
Corn-min (834)	32.44	25.03	26.55	31.04	36.11	28.29	28.90	28.28	33.86	28.11	32.10	29.68
Corn (234)	36.22	26.48	26.79	42.86	43.19	28.56	38.47	29.12	38.81	33.46	34.74	34.67
Grass/Pasture (497)	41.08	34.93	27.50	32.23	106.71	37.52	30.11	28.91	45.41	27.17	27.69	57.66
Grass/Trees (747)	30.32	27.23	24.12	36.52	31.42	25.12	30.05	26.46	26.41	23.51	23.25	28.72
Grass/pasture-mowed (26)	32.74	26.06	26.33	26.96	23.93	24.31	26.27	22.78	38.68	33.97	24.24	25.76
Hay-windrowed (489)	59.46	35.72	34.06	46.81	35.59	31.08	39.72	29.94	65.39	57.00	33.04	34.87
Oats (20)	26.04	25.73	23.27	25.53	25.33	25.65	24.72	23.14	25.39	25.31	23.68	24.22
Soybeans-notill (968)	47.07	22.55	24.11	31.58	51.32	26.72	33.60	31.02	27.59	24.49	26.37	25.01
Soybeans-min (2468)	46.08	24.93	27.10	33.71	48.28	31.98	34.01	31.93	36.13	28.93	33.45	31.14
Soybeans-clean (614)	45.09	23.89	24.52	49.26	54.35	25.31	44.59	29.82	31.76	26.97	26.96	25.85
Wheat (212)	29.58	31.16	26.77	29.20	27.18	25.81	26.36	33.12	26.99	26.19	29.65	27.36
Woods (1294)	50.21	51.99	27.81	27.86	91.95	47.18	36.88	38.05	40.84	37.01	42.88	49.38
Bldg-Grass-Trees (380)	43.97	45.95	30.04	33.32	34.73	39.05	32.49	35.61	33.09	33.02	35.73	35.98
Stone-steel towers (95)	93.62	70.79	49.52	61.11	98.25	36.43	36.12	105.28	92.80	36.84	56.67	45.32
Overall RMSE-based error	40.80	34.24	27.37	32.97	47.49	32.93	32.48	32.48	35.60	30.62	32.19	34.23

both the endmember extraction and the linear spectral unmixing stages. It should be noted that the same FCLS unmixing algorithm is always used to estimate the fractional abundances of different sets of endmembers produced by different algorithms with and without spatial preprocessing, thus allowing us to individually substantiate the impact of spatial preprocessing.

The metric employed to evaluate the goodness of the reconstruction is the RMSE between the original and reconstructed hyperspectral scenes, which can be defined as follows. Let us assume that $\mathbf{I}^{(O)}$ is the original hyperspectral scene and that $\mathbf{I}^{(R)}$ is a reconstructed version of $\mathbf{I}^{(O)}$, which was obtained using (1) with a set of endmembers and their corresponding FCLS-estimated fractional abundances. Let us also assume that the pixel vector at spatial coordinates (i, j) in the original hyperspectral scene is given by $\mathbf{X}^{(O)}(i, j) = [x_1^{(O)}(i, j), x_2^{(O)}(i, j), \dots, x_n^{(O)}(i, j)]$, whereas the corresponding pixel vector at the same spatial coordinates in the reconstructed hyperspectral scene is given by $\mathbf{X}^{(R)}(i, j) = [x_1^{(R)}(i, j), x_2^{(R)}(i, j), \dots, x_n^{(R)}(i, j)]$. With the preceding notation in mind, the RMSE between the original and reconstructed hyperspectral scenes is calculated as follows:

$$\text{RMSE}(\mathbf{I}^{(O)}, \mathbf{I}^{(R)}) = \frac{1}{s \times l} \sum_{i=1}^s \sum_{j=1}^l \left(\frac{1}{n} \sum_{k=1}^n [x_k^{(O)}(i, j) - x_k^{(R)}(i, j)]^2 \right)^{\frac{1}{2}}. \quad (10)$$

Table IV reports the overall RMSE scores calculated using (10) and also the individual per-class RMSE scores calculated

using only the spatial coordinates of the pixels labeled as belonging to a certain land-cover class in the ground-truth map available for the AVIRIS Indian Pines scene. In each reconstruction, we used the endmembers extracted by OSP, N-FINDR, and VCA with ($ws = 3$, $ws = 5$, and $ws = 9$) and without spatial preprocessing ($ws = 0$). From Table IV, it can be observed that spatial preprocessing allows a significant reduction in both the overall and individual RMSE scores. This is particularly the case for land-cover classes made up of homogeneous pixels (e.g., *Corn*, *Grass*, and *Soybeans*), whereas the land-cover classes mainly formed by anomalous pixels (e.g., the *Bldg-Grass-Trees* class) exhibit a less significant reduction in individual RMSE scores. This is expected as the preprocessing module privileges homogeneous areas. Finally, Table IV also reveals that the overall RMSE error after comparing the original scene with a reconstructed version using endmembers produced after spatial preprocessing was always lower than a reconstructed version without preprocessing, with $ws = 5$ shown as an example. The aforementioned observations are shown in Fig. 7, which graphically represents the per-pixel RMSE errors obtained after reconstructing the AVIRIS Indian Pines scene using the endmembers extracted by OSP, N-FINDR, and VCA from the original image [Fig. 7 (left column)] and from a preprocessed version using $ws = 5$ [Fig. 7 (right column)].

C. Experiment 3: AVIRIS Cuprite Scene

The number of endmembers p for the AVIRIS Cuprite scene was first estimated using the NWHFC method [32], where a reasonable estimate for the VD seemed to be 14 when false

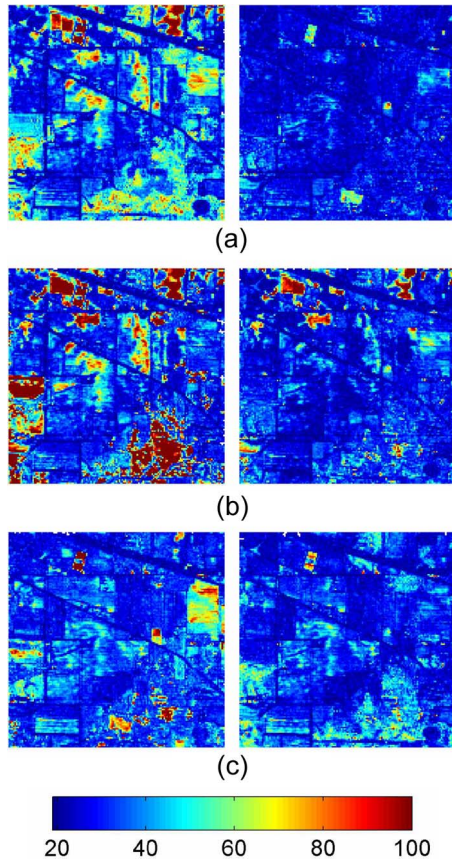


Fig. 7. RMSE-based reconstruction errors (in percentage, multiplied by a constant factor of 100) obtained after comparing the original AVIRIS Indian Pine scene with a reconstructed version of the same scene using the fully constrained linear mixture model in (1) and the endmembers extracted by the (a) OSP, (b) N-FINDR, and (c) VCA algorithms. Two cases are reported for each algorithm: (leftmost column) without spatial preprocessing and (rightmost column) with spatial preprocessing prior to endmember extraction, using a window size of $ws = 5$.

alarm probability P_F was set to 10^{-4} – 10^{-6} . As was already observed in our experiments with the AVIRIS Indian Pine scene in the previous section, the proposed spatial preprocessing did not significantly affect the estimation of the number of endmembers.

As a result, experiments in this section will be presented for a specific case study in which $p = 14$.

The only reference information available for the AVIRIS Cuprite scene is a USGS spectral library containing the most representative spectral signatures of the minerals present in the Cuprite mining district in Nevada.⁵ An experiment-based cross-examination of the algorithm endmember extraction accuracy is presented in Table V, which tabulates the SAD scores obtained after comparing the USGS library spectra, with the corresponding endmembers extracted by the considered endmember extraction algorithms, with ($ws > 0$) and without ($ws = 0$) spatial preprocessing.

⁵Reference information about the mapping of such materials in the Cuprite mining district using the Tetracorder method developed by the USGS is also available at <http://speclab.cr.usgs.gov/PAPERS/tetracorder>. However, the Tetracorder method also used the USGS library as a criterion for producing the mapping.

It should be noted that Table V was originally intended to display only the smallest SAD scores of all endmembers with respect to each USGS signature for each considered algorithm. The constraint imposed to establish the spectral matchings, where the term *matching* denotes the association of an endmember obtained by a certain algorithm with a single spectral signature in the USGS library, is that, once an endmember has been matched with a certain USGS signature, this signature is immediately removed from the library, so that subsequent endmember matchings are only possible with the remaining library spectra. As a result, a blank value in Table V indicates that the USGS spectrum could not be matched with any of the extracted endmembers. We are aware that this matching procedure is suboptimal in the sense that it may strongly depend on the order in which endmembers are matched (e.g., two or more endmembers may result in a minimum SAD distance value when compared with the same library signature, and in this case, the endmember that is matched in the first place may indeed affect subsequent matching of the remaining endmembers). In order to avoid this problem, all such matchings in our experiments have been performed by repeating the process 10 000 times, each one with a random rearrangement on the order of the 14 endmembers to be matched, thus randomizing the initial state of the process. As the final criterion, the best global match is considered to be the one with the minimum average SAD value across all runs. This criterion has been applied to all the endmember extraction algorithms tested in our experiments.

With the aforementioned considerations in mind, the quantitative results provided in Table V reveal that most of the relevant minerals in the USGS library can accurately be matched with spectral endmembers extracted by the different methods tested although some of the matchings involving minerals, such as *Alunite*, *Calcite*, *Pyrophyllite*, or *Sphene*, seem to be dependent on the algorithm and spatial preprocessing window used. The analysis reported in Table V also suggests that the use of spatial information can improve the overall accuracy of spectral matching, as can be observed by analyzing the average SAD scores reported in the last row of the table. Specifically, these average results reveal that the use of spatial information can improve the accuracy of spectral matchings in both the OSP and N-FINDR algorithms. It should be noted that the reference USGS signatures used for comparison were not actually collected in the Cuprite mining district, and this makes an assessment of the endmembers difficult. In order to analyze the preceding results in more detail and substantiate the impact of spatial preprocessing on the VCA algorithm, further experiments were conducted using the RMSE criterion (based on the reconstruction of the original image using extracted endmembers and their FCLSU-estimated fractional abundances), as described in previous sections.

Table VI shows the RMSE-based errors obtained after reconstructing the original AVIRIS Cuprite scene using the endmembers provided by different methods and their corresponding FCLSU-estimated fractional abundances, where (10) was used to produce the quantities reported in the table. As shown in Table VI, when the reconstruction was performed using the endmembers produced after spatial preprocessing ($ws > 0$),

TABLE V
SAD-BASED SPECTRAL SIMILARITY SCORES (MULTIPLIED BY A CONSTANT FACTOR OF 100) BETWEEN SPECTRAL SIGNATURES CONTAINED IN THE USGS LIBRARY AND THEIR CORRESPONDING ENDMEMBERS EXTRACTED FROM THE AVIRIS CUPRITE SCENE BY THREE DIFFERENT ALGORITHMS (OSP, N-FINDR, AND VCA) WITHOUT SPATIAL PREPROCESSING ($ws = 0$) AND WITH SPATIAL PREPROCESSING, USING WINDOW SIZES OF $ws = 3$, $ws = 5$, AND $ws = 9$

USGS Signature	OSP				NFINDR				VCA			
	$ws = 0$	$ws = 3$	$ws = 5$	$ws = 9$	$ws = 0$	$ws = 3$	$ws = 5$	$ws = 9$	$ws = 0$	$ws = 3$	$ws = 5$	$ws = 9$
Alunite GDS84	7.67	11.94	-	-	-	9.45	-	-	-	10.45	10.45	-
Alunite GDS82	8.00	6.52	7.26	7.26	6.87	10.90	7.21	8.00	6.47	-	-	6.47
Alunite AL706	19.49	-	16.40	-	19.49	-	14.73	15.51	-	16.40	-	18.59
Buddingtonite GDS85	10.17	10.17	10.17	10.17	7.21	8.33	10.17	10.17	10.17	10.17	10.17	10.17
Calcite WS272	10.03	10.03	10.03	10.03	9.48	10.03	9.99	-	9.48	10.44	10.44	-
Kaolinite KGa-1	10.22	10.22	10.22	10.22	10.22	10.22	10.22	10.22	19.70	17.03	22.83	17.78
Muscovite GDS107	11.06	10.40	12.55	9.80	11.18	12.86	12.82	16.02	10.08	12.38	13.38	12.38
Muscovite GDS108	10.07	10.07	10.22	9.90	9.79	9.79	9.41	9.91	12.78	9.29	13.04	9.80
Muscovite GDS111	21.58	21.58	14.32	21.58	18.06	21.58	16.71	14.71	15.53	13.44	13.44	15.39
Jarosite GDS99	19.22	18.37	20.31	16.22	18.95	16.22	20.31	14.79	16.22	19.53	16.22	15.48
Montmorillonite SWy-1	10.68	8.28	6.95	6.95	11.39	12.60	9.53	7.28	11.97	17.43	11.41	18.48
Pyrophyllite PYS1A	-	-	-	13.79	-	-	-	22.18	21.42	-	21.42	24.24
Chalcedony CU91-6A	7.77	8.05	7.77	9.94	11.40	8.05	9.94	11.40	12.39	17.24	11.19	3.53
Andradite GDS12	18.60	18.04	13.93	18.04	13.26	13.06	7.22	11.83	7.31	10.55	7.73	7.31
Dumortierite HS190.3B	11.95	10.19	11.27	8.96	11.28	9.33	11.27	13.18	11.25	11.25	11.25	11.28
Sphene HS189.3B	-	5.20	8.44	8.44	9.05	7.34	8.59	12.05	8.13	5.20	5.07	6.79
Average	12.61	11.36	11.42	11.52	11.97	11.41	11.29	12.66	12.35	12.91	12.72	12.69

TABLE VI
OVERALL RMSE-BASED RECONSTRUCTION ERRORS (MULTIPLIED BY A CONSTANT FACTOR OF 100) OBTAINED AFTER COMPARING THE ORIGINAL AVIRIS CUPRITE SCENE WITH A RECONSTRUCTED VERSION OF THE SAME SCENE USING THE FULLY CONSTRAINED LINEAR MIXTURE MODEL IN (1) AND THE ENDMEMBERS EXTRACTED BY OSP, N-FINDR, AND VCA ALGORITHMS. TWO CASES ARE REPORTED FOR EACH ALGORITHM: WITHOUT SPATIAL PREPROCESSING ($ws = 0$) AND WITH SPATIAL PREPROCESSING PRIOR TO ENDMEMBER EXTRACTION, USING WINDOW SIZES OF $ws = 3$, $ws = 5$, $ws = 7$, $ws = 9$, AND $ws = 11$

Algorithm	$ws = 0$	$ws = 3$	$ws = 5$	$ws = 7$	$ws = 9$	$ws = 11$
OSP	4.791	1.862	1.836	2.656	2.656	3.538
N-FINDR	0.652	0.570	0.548	0.645	0.725	0.545
VCA	0.744	0.608	0.385	0.451	0.768	0.785

the RMSE errors were lower for all considered algorithms, although a degradation in performance was generally observed when the size of the preprocessing window was $ws = 7$ or higher. These results may be due to the low spatial resolution of the AVIRIS Cuprite scene (20-m pixels), leading us to believe that very large window sizes may not be as effective in characterizing the spatial-spectral information contained in low spatial resolution hyperspectral scenes. In addition, the effectiveness of the preprocessing is likely scene dependent, in the sense that it may be more effective with scenes containing homogeneous regions.

Fig. 8 shows the per-pixel RMSE errors obtained after reconstructing the original image using the endmembers obtained by different algorithm images (leftmost column) and also the

reconstruction errors using endmembers obtained after spatial preprocessing using a window with a size of $ws = 5$ (rightmost column). As it was also the case with the AVIRIS Indian Pines scene, the three endmember extraction algorithms shown in Fig. 8 (i.e., OSP, N-FINDR, and VCA) resulted in lower per-pixel RMSE errors when the proposed spatial preprocessing technique was used prior to the endmember extraction stage.

Finally, as an indication of the preprocessing time required by our proposed module, if we consider a spatial element of window size $ws = 5$ pixels, the proposed method (implemented in Matlab) takes about 92 s to preprocess the considered AVIRIS Cuprite scene in a desktop computer with a CPU clock of 2.4 GHz and 2 GB of random access memory.

V. CONCLUSION AND FUTURE RESEARCH LINES

The incorporation of spatial information into the process of extracting endmembers from hyperspectral image data sets has been a long-awaited goal by the remote-sensing community. Several well-known algorithms have been used for the task of extracting endmembers by considering only the spectral properties of the data when conducting the search. However, there is a need to incorporate the spatial arrangement of the data in the development of endmember extraction and spectral unmixing algorithms.

The main contribution of this paper is the development of a simple yet effective methodology that simultaneously integrates both the spatial and spectral sources of information contained in the hyperspectral data. The proposed method allows for

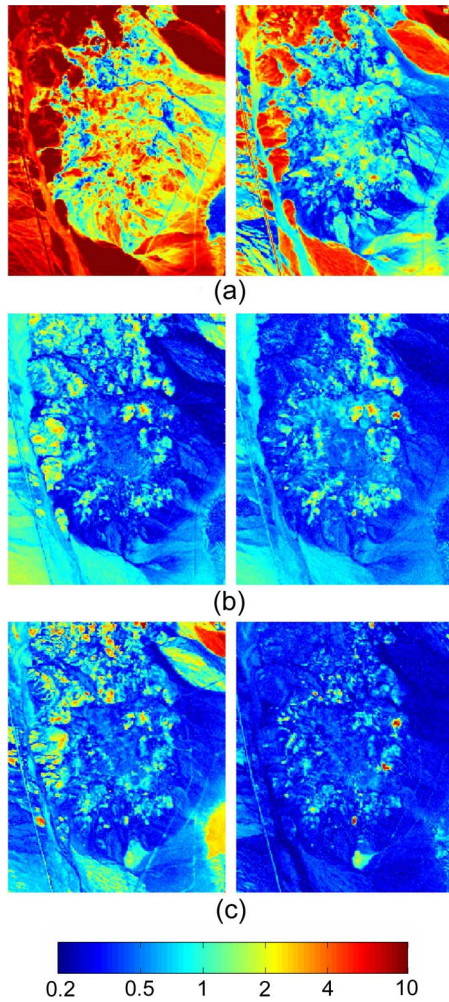


Fig. 8. RMSE-based reconstruction errors (multiplied by a constant factor of 100) obtained after comparing the original AVIRIS Cuprite scene with a reconstructed version of the same scene using the fully constrained linear mixture model in (1) and the endmembers extracted by the (a) OSP, (b) N-FINDR, and (c) VCA algorithms. Two cases are reported for each algorithm: (leftmost column) without spatial preprocessing and (rightmost column) spatial preprocessing prior to endmember extraction, using a window size of $ws = 5$.

the incorporation of spatial information into existing image spectral-based endmember extraction algorithms, without the need for these algorithms to be modified. Instead, the proposed approach works as an independent but complementary spatial preprocessing module for endmember extraction using the standard hyperspectral processing chain.

Our experiments, using both simulated and real data sets, revealed that the proposed approach is quite promising in the sense that it can take advantage of spatial information in order to intelligently guide the traditional spectral-based approach to extract endmembers from a hyperspectral scene. An advantage of the proposed approach is that the only required input parameter for spatial preprocessing, i.e., size ws of the spatial window, is not a critical parameter that requires fine-tuning. Our experimental results also indicate that the physical representation (via a fully constrained linear mixture model) of a set of endmembers extracted using spatial-spectral information and their corresponding abundance fractions can be used to provide a good reconstruction of the original data.

This approach allowed us to evaluate the effect of the proposed preprocessing framework using a simple reconstruction-based approach, which does not require detailed ground-truth information about the original scene, which is generally very costly to obtain in terms of time and finance. The results obtained in our experiments indicate that the linear mixture model, when improved by the integration of spatial and spectral information in the task of selecting endmembers, is able to provide a relatively good characterization of general landscape conditions in two highly representative AVIRIS hyperspectral scenes, which have thoroughly been studied in the literature.

Despite the aforementioned remarks, further experimentation should be conducted in future work to address some unresolved issues that may present challenges over time. Specifically, we are planning on incorporating a two-filter strategy in our implementation that looks at both highly homogeneous regions and single pixels that are distinct from their surroundings (anomalous pixels), with both having increased weight in the search for endmembers. An evaluation of different distance measures to be used in the extension of the proposed preprocessing framework is another key topic that deserves future research. In addition, tests with alternative spatial-weighting formulations should also be conducted. It would also be useful to explore the behavior of the proposed preprocessing method in cases where the linear mixture model assumption is no longer valid to describe the mixing systematics of the observed materials, thus conducting a more detailed evaluation of linear versus nonlinear mixture models in different application domains. An investigation of the use of the proposed methodology in conjunction with source separation techniques, such as those described in [33], is also a topic that deserves future research. Finally, efficient parallel implementations based on high-performance computing architectures are being currently tested at our laboratory in order to provide the proposed methodology with real-time capabilities.

ACKNOWLEDGMENT

The authors would like to thank Dr. R. O. Green and Dr. D. A. Landgrebe for sharing the AVIRIS Cuprite and Indian Pines data sets with the scientific community, Dr. J. Bioucas-Dias and Dr. J. Nascimento for making their implementation of the VCA algorithm available as freeware, and the anonymous reviewers for their comments and suggestions, which greatly helped improve the quality and presentation of this paper.

REFERENCES

- [1] A. F. H. Goetz, G. Vane, J. E. Solomon, and B. N. Rock, "Imaging spectrometry for Earth remote sensing," *Science*, vol. 228, no. 4704, pp. 1147–1153, Jun. 1985.
- [2] R. O. Green, M. L. Eastwood, C. M. Sarture, T. G. Chrien, M. Aronsson, B. J. Chippendale, J. A. Faust, B. E. Pavri, C. J. Chovit, M. Solis, K. A. Monsch, M. R. Olah, and O. Williams, "Imaging spectroscopy and the Airborne Visible/Infrared Imaging Spectrometer (AVIRIS)," *Remote Sens. Environ.*, vol. 65, no. 3, pp. 227–248, Sep. 1998.
- [3] D. A. Landgrebe, *Signal Theory Methods in Multispectral Remote Sensing*. New York: Wiley, 2003.
- [4] C.-I. Chang, *Hyperspectral Imaging: Techniques for Spectral Detection and Classification*. New York: Kluwer, 2003.
- [5] C.-I. Chang, *Hyperspectral Data Exploitation: Theory and Applications*. New York: Wiley, 2007.

- [6] N. Keshava and J. F. Mustard, "Spectral unmixing," *IEEE Signal Process. Mag.*, vol. 19, no. 1, pp. 44–57, Jan. 2002.
- [7] J. B. Adams, M. O. Smith, and P. E. Johnson, "Spectral mixture modeling: A new analysis of rock and soil types at the Viking Lander 1 site," *J. Geophys. Res.*, vol. 91, no. B8, pp. 8098–8112, Jul. 1986.
- [8] A. Plaza, P. Martinez, R. Perez, and J. Plaza, "A quantitative and comparative analysis of endmember extraction algorithms from hyperspectral data," *IEEE Trans. Geosci. Remote Sens.*, vol. 42, no. 3, pp. 650–663, Mar. 2004.
- [9] J. W. Boardman, F. A. Kruse, and R. O. Green, "Mapping target signatures via partial unmixing of AVIRIS data," in *Proc. JPL Airborne Earth Sci. Workshop*, 1995, pp. 23–26.
- [10] M. E. Winter, "N-FINDR: An algorithm for fast autonomous spectral end-member determination in hyperspectral data," in *Proc. SPIE Image Spectrometry V*, 2003, vol. 3753, pp. 266–277.
- [11] R. A. Neville, K. Staenz, T. Szeredi, J. Lefebvre, and P. Hauff, "Automatic endmember extraction from hyperspectral data for mineral exploration," in *Proc. 21st Can. Symp. Remote Sens.*, 1999, pp. 21–24.
- [12] J. H. Bowles, P. J. Palmadesso, J. A. Antoniadis, M. M. Baumbach, and L. J. Rickard, "Use of filter vectors in hyperspectral data analysis," in *Proc. SPIE Infrared Spaceborne Remote Sens. III*, 1995, vol. 2553, pp. 148–157.
- [13] A. Ifarraguerri and C.-I. Chang, "Multispectral and hyperspectral image analysis with convex cones," *IEEE Trans. Geosci. Remote Sens.*, vol. 37, no. 2, pp. 756–770, Mar. 1999.
- [14] J. C. Harsanyi and C.-I. Chang, "Hyperspectral image classification and dimensionality reduction: An orthogonal subspace projection," *IEEE Trans. Geosci. Remote Sens.*, vol. 32, no. 4, pp. 779–785, Jul. 1994.
- [15] M. Berman, H. Kiiveri, R. Lagerstrom, A. Ernst, R. Dunne, and J. F. Huntington, "ICE: A statistical approach to identifying endmembers in hyperspectral images," *IEEE Trans. Geosci. Remote Sens.*, vol. 42, no. 10, pp. 2085–2095, Oct. 2004.
- [16] L. Miao and H. Qi, "Endmember extraction from highly mixed data using minimum volume constrained nonnegative matrix factorization," *IEEE Trans. Geosci. Remote Sens.*, vol. 45, no. 3, pp. 765–777, Mar. 2007.
- [17] C.-I. Chang, C.-C. Wu, W. Liu, and Y.-C. Ouyang, "A new growing method for simplex-based endmember extraction algorithm," *IEEE Trans. Geosci. Remote Sens.*, vol. 44, no. 10, pp. 2804–2819, Oct. 2006.
- [18] J. Wang and C.-I. Chang, "Applications of independent component analysis in endmember extraction and abundance quantification for hyperspectral imagery," *IEEE Trans. Geosci. Remote Sens.*, vol. 44, no. 9, pp. 2601–2616, Sep. 2006.
- [19] A. Plaza and C.-I. Chang, "Impact of initialization on design of endmember extraction algorithms," *IEEE Trans. Geosci. Remote Sens.*, vol. 44, no. 11, pp. 3397–3407, Nov. 2006.
- [20] C.-I. Chang and A. Plaza, "A fast iterative algorithm for implementation of pixel purity index," *IEEE Geosci. Remote Sens. Lett.*, vol. 3, no. 1, pp. 63–67, Jan. 2006.
- [21] A. Zare and P. Gader, "Hyperspectral band selection and endmember detection using sparsity promoting priors," *IEEE Geosci. Remote Sens. Lett.*, vol. 5, no. 2, pp. 256–260, Apr. 2008.
- [22] A. Plaza, P. Martinez, R. Perez, and J. Plaza, "Spatial/spectral endmember extraction by multidimensional morphological operations," *IEEE Trans. Geosci. Remote Sens.*, vol. 40, no. 9, pp. 2025–2041, Sep. 2002.
- [23] A. Plaza, P. Martinez, J. Plaza, and R. Perez, "Dimensionality reduction and classification of hyperspectral image data using sequences of extended morphological transformations," *IEEE Trans. Geosci. Remote Sens.*, vol. 43, no. 3, pp. 466–479, Mar. 2005.
- [24] D. M. Rogge, B. Rivard, J. Zhang, A. Sanchez, J. Harris, and J. Feng, "Integration of spatial-spectral information for the improved extraction of endmembers," *Remote Sens. Environ.*, vol. 110, no. 3, pp. 287–303, Oct. 2007.
- [25] R. A. Schowengerdt, *Remote Sensing: Models and Methods for Image Processing*, 2nd ed. New York: Academic, 1997.
- [26] D. Heinz and C.-I. Chang, "Fully constrained least squares linear mixture analysis for material quantification in hyperspectral imagery," *IEEE Trans. Geosci. Remote Sens.*, vol. 39, no. 3, pp. 529–545, Mar. 2001.
- [27] J. M. P. Nascimento and J. M. Bioucas-Dias, "Vertex component analysis: A fast algorithm to unmix hyperspectral data," *IEEE Trans. Geosci. Remote Sens.*, vol. 43, no. 4, pp. 898–910, Apr. 2005.
- [28] A. A. Green, M. Berman, P. Switzer, and M. D. Craig, "A transformation for ordering multispectral data in terms of image quality with implications for noise removal," *IEEE Trans. Geosci. Remote Sens.*, vol. 26, no. 1, pp. 65–74, Jan. 1988.
- [29] R. N. Clark, G. A. Swayze, K. E. Livo, R. F. Kokaly, S. J. Sutley, J. B. Dalton, R. R. McDougal, and C. A. Gent, "Imaging spectroscopy: Earth and planetary remote sensing with the USGS tetracorder and expert systems," *J. Geophys. Res.*, vol. 108, no. E12, pp. 1–44, Dec. 2003.
- [30] G. Swayze, R. N. Clark, F. Kruse, S. Sutley, and A. Gallagher, "Ground-truthing AVIRIS mineral mapping at Cuprite, Nevada," in *Proc. JPL Airborne Earth Sci. Workshop*, 1992, pp. 47–49.
- [31] G. E. P. Box, W. G. Hunter, and J. S. Hunter, *Statistics for Experimenters: An Introductory to Design Data Analysis and Model Building*. New York: Wiley, 1978.
- [32] C.-I. Chang and Q. Du, "Estimation of number of spectrally distinct signal sources in hyperspectral imagery," *IEEE Trans. Geosci. Remote Sens.*, vol. 42, no. 3, pp. 608–619, Mar. 2004.
- [33] S. Moussaoui, H. Hauksdottir, F. Schmidt, C. Jutten, J. Chanussot, D. Brie, S. Doute, and J. Benediktsson, "On the decomposition of Mars hyperspectral data by ICA and Bayesian positive source separation," *Neurocomputing*, vol. 71, no. 10–12, pp. 2194–2208, Jun. 2008.



Maciel Zortea received the Civil Engineer degree and the M.Sc. degree in remote sensing from the Federal University of Rio Grande do Sul, Porto Alegre, Brazil, in 2002 and 2004, respectively, and the Ph.D. degree in information and communication science and technologies, curriculum in space science and engineering from the University of Genoa, Genoa, Italy, in 2007.

He was a Marie Curie Experienced Researcher within the Hyperspectral Imaging Network. He is currently a Postdoctoral Researcher with the Department of Technology of Computers and Communications, University of Extremadura, Caceres, Spain. His research interests include image processing and pattern recognition methodologies for remote-sensing applications, with particular interest in endmember extraction and spectral unmixing, hyperspectral image analysis, classification, and geophysical parameter estimation from remotely sensed data.

Dr. Zortea has served as a Reviewer for several journals, including the IEEE TRANSACTIONS ON GEOSCIENCE AND REMOTE SENSING.



Antonio Plaza (M'05–SM'07) received the M.S. and Ph.D. degrees in computer engineering from the University of Extremadura, Caceres, Spain, in 1997 and 2002, respectively.

He was a Visiting Researcher with the Remote Sensing Signal and Image Processing Laboratory, University of Maryland Baltimore County, Baltimore; the Applied Information Sciences Branch, Goddard Space Flight Center, Greenbelt, MD; and the AVIRIS Data Facility, JPL, Pasadena, CA. Since 2000, he has been an Associate Professor with the Department of Technology of Computers and Communications, University of Extremadura, where he was an Assistant Professor from 1997 to 1999. He is the Coordinator of the Hyperspectral Imaging Network (Hyper-I-Net), which is a European project designed to build an interdisciplinary research community focused on hyperspectral imaging activities. He has been a Proposal Reviewer for the European Commission, the ESA, and the Spanish Government, and has also served as a reviewer for more than 30 different journals. He is the author or coauthor of more than 150 publications on remotely sensed hyperspectral imaging, including journal papers, book chapters, and conference proceeding papers. He has coedited a book on high-performance computing in remote sensing and several special issues on remotely sensed hyperspectral imaging for different journals. His research interests include remotely sensed hyperspectral imaging, pattern recognition, signal and image processing, and efficient implementation of large-scale scientific problems on parallel and distributed computer architectures.

Dr. Plaza is an Associate Editor for the IEEE TRANSACTIONS ON GEOSCIENCE AND REMOTE SENSING on hyperspectral image analysis and signal processing. He has served as a Reviewer for more than 90 manuscripts submitted to this journal.